photonics

MDPI

Article

Broadband Source-Surrounded Cloak for On-Chip Antenna Radiation Pattern Protection

Weifeng Han [1], Hanchuan Chen [1], Fei Sun [1,*], Yichao Liu [1] and Shuai Zhang [2]

[1] Key Lab of Advanced Transducers and Intelligent Control System, Ministry of Education and Shanxi Province, College of Physics and Optoelectronics Engineering, Taiyuan University of Technology, Taiyuan 030024, China; 15981673627@139.com (W.H.); hanchuan.chen2000@gmail.com (H.C.); liuyichao@tyut.edu.cn (Y.L.)

[2] Department of Electronic Systems, Aalborg University, 9220 Aalborg, Denmark; sz@es.aau.dk

* Correspondence: sunfei@tyut.edu.cn

Abstract

With the expansion of electromagnetic wave communication frequency bands and the improvement of integrated circuit integration, electromagnetic waves emitted by on-chip antennas are easily scattered by electronic components, causing radiation pattern distortion, which limits the improvement of integration and communication stability. Traditional cloaks can reduce electromagnetic scattering, but they cannot achieve broadband and omnidirectional performance simultaneously, and are mostly designed for external sources, making it difficult to protect on-chip antenna radiation patterns. In this work, a broadband air-impedance-matched metamaterial (AIMM) with characteristic impedance matched to free space is proposed in 2–8 GHz, with geometry-tunable phase delay and transmittance higher than 93%. Based on AIMM, a broadband source-surrounded cloak (SSC) is designed, which can guide electromagnetic waves from the surrounded source to bypass obstacles in any direction and restore the original wavefront outside the cloak, so as to protect the radiation pattern from scattering distortion. Numerical simulations show that the SSC works well in the whole bandwidth and remains effective when the source is offset. This work has important potential for improving the integration of integrated circuits and the stability of communication systems.

Keywords: broadband cloak; metamaterial; electromagnetic scattering suppression; radiation pattern protection; on-chip antenna

1. Introduction

Improving electromagnetic wave emission efficiency has become a critical technological objective with diverse applications. In particular, on-chip communication systems benefit from it, resulting in enhanced signal quality and increased transmission reliability [1–4]. However, as the component integration of on-chip communication systems continues to increase and the communication frequency bands expand, the electromagnetic waves emitted by on-chip antennas are prone to scattering by electronic components/metallic electronic components [5,6]. This scattering will cause distortion in the radiation pattern, ultimately leading to reduced electromagnetic wave emission efficiency. To balance electromagnetic wave emission efficiency, further improvement in the integration of on-chip communication systems has been limited. Traditional cloaks can be applied around electronic components to reduce their scattering of incident waves from the outside [7–10]. In recent years, an

Check for updates

Received: 28 May 2026
Revised: 20 June 2026
Accepted: 23 June 2026
Published: 24 June 2026

Copyright: © 2026 by the authors. Licensee MDPI, Basel, Switzerland. This article is an open access article distributed under the terms and conditions of the Creative Commons Attribution (CC BY) license.

increasing number of invisibility mechanisms and methods have been proposed. Notable research works in this field include cloaks based on transformation optics [11–15], cloaks based on optical conformal transformation [16–19], and cloaks based on scattering-cancelation; [20–25] et al. However, current cloaks are affected by two critical problems that limit their application in protecting the radiation patterns of on-chip sources within highly integrated on-chip communication systems. First, there is a significant bandwidth limitation. Most full-space cloaks operate only at single frequencies or narrow frequency bands [26–28]. Although directionally restricted cloaks [29,30] or carpet cloaks may achieve broadband operation [31–35], they are not suitable for protecting the radiation patterns of on-chip sources or antennas. Second, all traditional cloaks are designed for electromagnetic waves incident from the outside to encounter concealed regions, but they do not address scenarios where electromagnetic waves generated by internal sources propagate outward and encounter concealed regions containing strong electromagnetic scatterers. Therefore, there is still a lack of a cloak that allows electromagnetic waves emitted in any propagation direction to bypass obstacles without scattering and operates across a broadband frequency range, thus protecting the radiation patterns of on-chip sources/antennas from distortion caused by surrounding electronic components. Advanced computational design methodologies, particularly topology optimization and its adjoint formulations, have emerged as powerful tools for inverse design of electromagnetic metamaterials and cloaking devices [36–38].

In recent years, the rapid development of novel metadevice-based metamaterials/metasurfaces [39]—including extreme-parameter metamaterials [30], reconfigurable metadevices [40], multiphysics metadevices [41,42], diffusion metamaterials [43–45], time-varying and space–time-coding metamaterials [46–50], as well as active and non-Hermitian metamaterials [51–55]—has provided new routes toward advanced cloaking design. Motivated by these progresses, we propose a new solution to realize broadband, omnidirectional radiation pattern protection for on-chip antennas against scattering distortion from nearby electronic components. In this work, a broadband air-impedance-matched metamaterial (AIMM) operating over the 2–8 GHz bandwidth is proposed, achieving a tunable-by-design effective refractive index ranging from 1.1 to 1.5. This adjustability is achieved by adjusting the dielectric mixing ratio m, while maintaining a transmittance t above 93% across the entire bandwidth. We further propose a broadband source-surrounded cloak (SSC) based on AIMM for on-chip radiation pattern protection. The SSC operates with a bandwidth of 6 GHz centered at f_0 = 5 GHz (λ_0 = 60 mm). As illustrated in Figure 1, the SSC fundamentally differs from traditional cloaks by surrounding the source rather than the scatterer. Electronic components can be placed within the concealed regions, while broadband electromagnetic waves emitted omnidirectionally from the source are guided by the SSC to bypass the components without scattering. Crucially, the electromagnetic waves fully reproduce their original wavefronts after exiting the cloak. The SSC concept opens several promising avenues. First, 3D extension would enable protection for vertically oriented dipoles and complex antenna configurations, essential for fully integrated chip architectures. Second, experimental verification with fabricated AIMM samples is underway to validate broadband performance under realistic conditions. Third, the broadband AIMM methodology can be extended to millimeter-wave and terahertz regimes. Potential applications include 5G/6G on-chip communication, IoT devices, and high-performance computing modules.

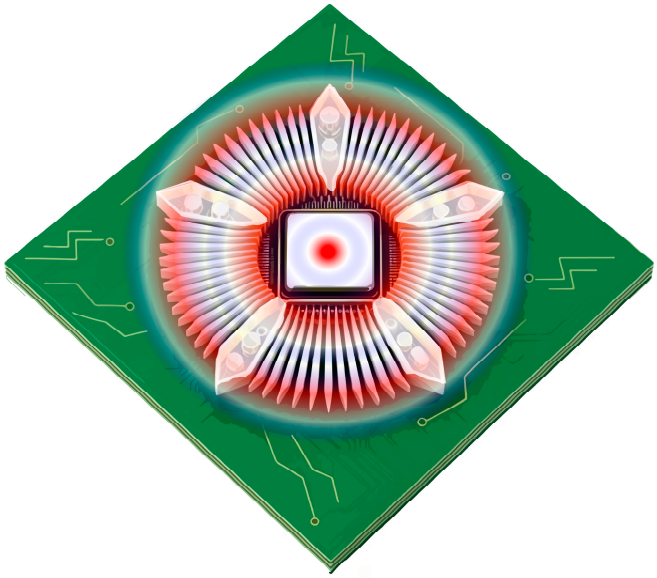


Figure 1. The schematic view of SSC applied to on-chip communication system. It demonstrates the on-chip antenna surrounded by SSC, with obstacles like electronic components that can scatter electromagnetic waves placed in the concealed regions of SSC. The electromagnetic waves emitted by the on-chip antenna in any propagation direction are guided around the obstacles by SSC and exit without distortion.

2. Materials and Methods

In this work, we consider transverse magnetic (TM) waves where the electric field E is polarized in the in-plane direction (perpendicular to the metal walls), the magnetic field H is oriented in the out-of-plane direction (perpendicular to the chip plane), and the wave vector k propagates radially. The metal walls act as perfect electric conductor (PEC) boundaries in the direction normal to the electric field (i.e., along the wall normal). Figure 2a details the structure of the AIMM, comprising top and bottom metal walls (treated as perfect electric conductor boundaries at microwave frequencies) sandwiching two symmetrical dielectric regions with relative permittivity ε_{rd}. The AIMM operates effectively solely for transverse magnetic (TM) waves, and accordingly, this work is confined to TM-polarized electromagnetic phenomena. The AIMM, with total height h_1, is partitioned along the radial direction into three functional sections: l_1 and l_3 serving as impedance-matching sections with gradually varying dielectric thickness from 0 to h, flanking the central l_2 section with constant dielectric thickness h. The dielectric mixing ratio $m = 2h/h_1$ in each channel is determined by the optical path-matching condition, ensuring that all channels have equal optical path lengths. The impedance-matching sections l_1 and l_3 provide smooth impedance transition between adjacent channels and the external free space, minimizing reflections at the interfaces. It should be emphasized that the AIMM structure is inherently anisotropic due to the metal walls confining the wave propagation; therefore, describing the system with a single scalar effective refractive index is physically inappropriate. The broadband behavior originates from the geometry-controlled optical path lengths rather than from any frequency-independent effective medium response. As shown in Figure 2c, the transmittance $t = |S_{21}|^2$ of the AIMM unit cell remains above 93% across the 2–8 GHz bandwidth under the parameters $l_1 = 0.02\lambda_0$, $l_2 = 0.02\lambda_0$, $l_3 = 0.02\lambda_0$, $h_1 = 0.02\lambda_0$, and $\varepsilon_{rd} = 10$ (e.g., Al_2O_3 [56]), with the dielectric mixing ratio m increasing from 0.25 to 0.75.

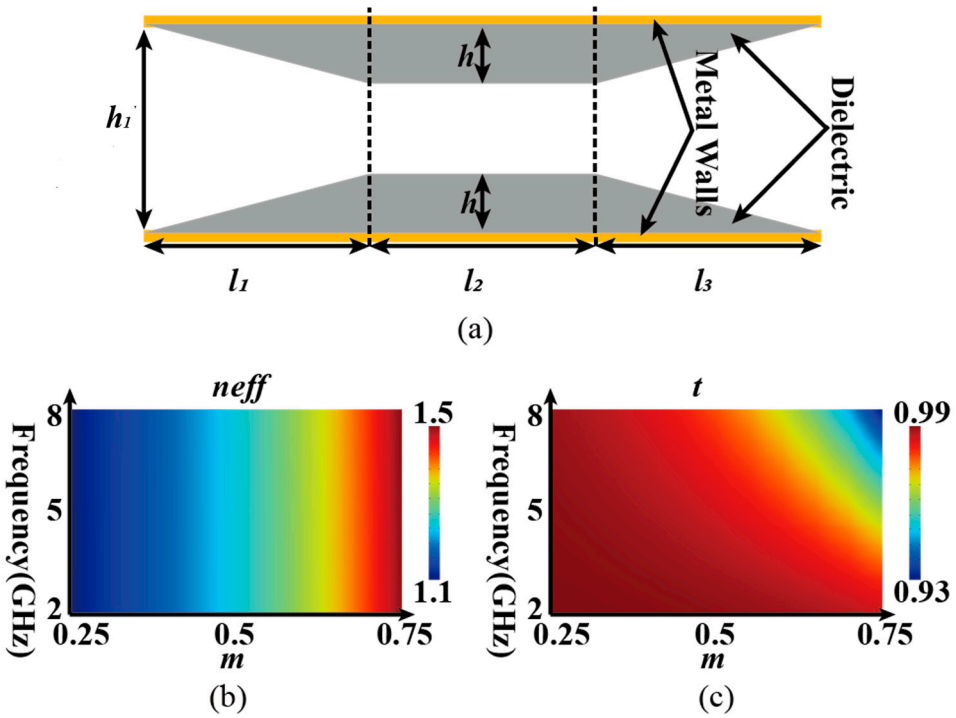


Figure 2. The design of AIMM. (**a**) The structural schematic diagram of AIMM. The yellow lines represent metal walls, and the gray areas are dielectric regions; (**b**) phase delay per unit cell as a function of $m = 2h/h_1$ and the frequency, shown for qualitative reference; (**c**) transmittance t as a function of $m = 2h/h_1$ and the frequency. In (**b**,**c**), $l_1 = 0.02\lambda_0$, $l_2 = 0.02\lambda_0$, $l_3 = 0.02\lambda_0$, $h_1 = 0.02\lambda_0$, and the relative permittivity of dielectric regions $\varepsilon_{rd} = 10$.

It should be noted that the 'broadband' characteristic of AIMM refers to the geometry-controlled broadband performance achieved through the mixing ratio m. Since the optical path length in each channel is determined solely by the physical geometry (m and channel length d_i) rather than by resonant effects, the waveguiding performance is inherently broadband. Alumina exhibits a relative permittivity variation of less than 3% across 2–8 GHz, which has negligible impact on the optical path matching. The metal walls approximate PEC boundaries at microwave frequencies with negligible skin depth effects. The broadband performance is therefore dominated by structural parameters (m, l_1, l_3) rather than material chromatic dispersion, consistent with subwavelength metal-channel cloaks. The reflection losses in the multi-channel SSC are suppressed by the impedance-matching sections l_1 and l_3, and the inter-channel coupling is negligible under the subwavelength condition; consequently, the overall radiation pattern protection performance is primarily determined by the optical path-matching accuracy rather than cumulative losses.

Figure 3 illustrates the SSC constructed from a series of AIMM within a cylindrical coordinate system. Electromagnetic waves emitted omnidirectionally from the SSC-surrounded source are guided by the AIMM array to bypass obstacles while precisely reproducing their original wavefronts outside the SSC. Using fivefold rotational symmetry, we detail the design of a 72° sector (1/5 of the full structure), with identical remaining sectors generated via rotational duplication. First, the AIMM channels are arranged in a cylindrical configuration with radially varying lengths. As an example, set $a = 0.5\lambda_0$, $b = 0.75\lambda_0$, $c = 1.25\lambda_0$, and $d = 1.5\lambda_0$. The angle θ occupied by each channel linearly decreases from 6° at a to 5° at b, remains at 5° from b to c, and then linearly increases back to 6° from c to d. The selection of θ must satisfy the subwavelength condition at the highest operating frequency. Five hexagonal concealed regions surrounded by metal walls can be generated via rotational symmetry (the green areas in Figure 3). Since the lengths of the channels are inconsistent,

to ensure the wavefront shape remains unchanged, the dielectric mixing ratio m is adjusted to equalize the optical path length d_i (i = 1, 2, 3, . . ., 12, representing the channel number) through the condition

$$d_i = n_{eff}^i L_i = constant. \quad (1)$$

The optical path length d_i for all channels is set to $3/2\lambda_0$. According to (1), the dielectric mixing ratio m and structural parameters l_1, l_2, and l_3 of the AIMMs in each channel are calculated and summarized in Table 1. The transmittance of each channel remains above 93% across the entire bandwidth (Figure 2c), confirming the impedance-matching design.

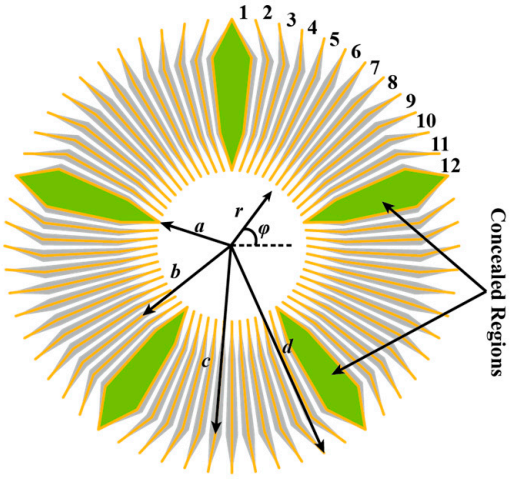


Figure 3. The structural schematic diagram of SSC. The green areas represent the concealed regions.

Table 1. The AIMM parameters for the SSC in Figure 3.

Channel Number	m	l_1 (mm)	l_2 (mm)	l_3 (mm)
1	0.7054	15.411	30.000	16.957
2	0.7170	15.278	30.000	16.341
3	0.7262	15.170	30.000	15.831
4	0.7332	15.088	30.000	15.438
5	0.7379	15.034	30.000	15.170
6	0.7402	15.006	30.000	15.034
7	0.7402	15.006	30.000	15.034
8	0.7379	15.034	30.000	15.170
9	0.7332	15.088	30.000	15.438
10	0.7262	15.170	30.000	15.831
11	0.7170	15.278	30.000	16.341
12	0.7054	15.411	30.000	16.957

3. Results

Figure 4 presents numerical simulations of the SSC conducted with COMSOL Multiphysics 6.3 (License #9406999) with its two-dimensional (2D) Wave Optics module. The simulation domain was set to a square region with side length 450 mm. Perfect electric conductor (PEC) boundaries were applied to the metal walls. Free triangular mesh was employed for domain discretization. The overall performance of the SSC is evaluated by the wavefront restoration quality rather than a single transmittance value, since the transmittance varies slightly among channels due to their different structural parameters, yet all channels maintain high transmittance characteristics. The simulation domain is limited to a $6.5\lambda_0 \times 6.5\lambda_0$ square region surrounded by perfect matched layers of thickness $0.5\lambda_0$, centered on a 1 V magnetic point source. Figure 4a shows the normalized magnetic field

distribution of a free-space magnetic point source without obstacles, exhibiting ideal cylindrical wavefronts at 2, 4, 6, and 8 GHz. Figure 4b shows the same source surrounded by five PEC obstacles (matching the concealed region geometry), where strong radiation pattern distortions caused by PEC scattering are observed, exacerbated at shorter wavelengths. Figure 4c demonstrates the source surrounded by the SSC with the same five PEC obstacles placed in the concealed regions. Here, electromagnetic waves emitted omnidirectionally from the source are guided by the SSC to bypass the obstacles and reproduce cylindrical wavefronts at the outer boundary of the SSC across the entire 6 GHz bandwidth. These results validate that the SSC effectively protects the radiation pattern of broadband sources from scattering by obstacles, regardless of emission direction or operating frequency within the designed bandwidth.

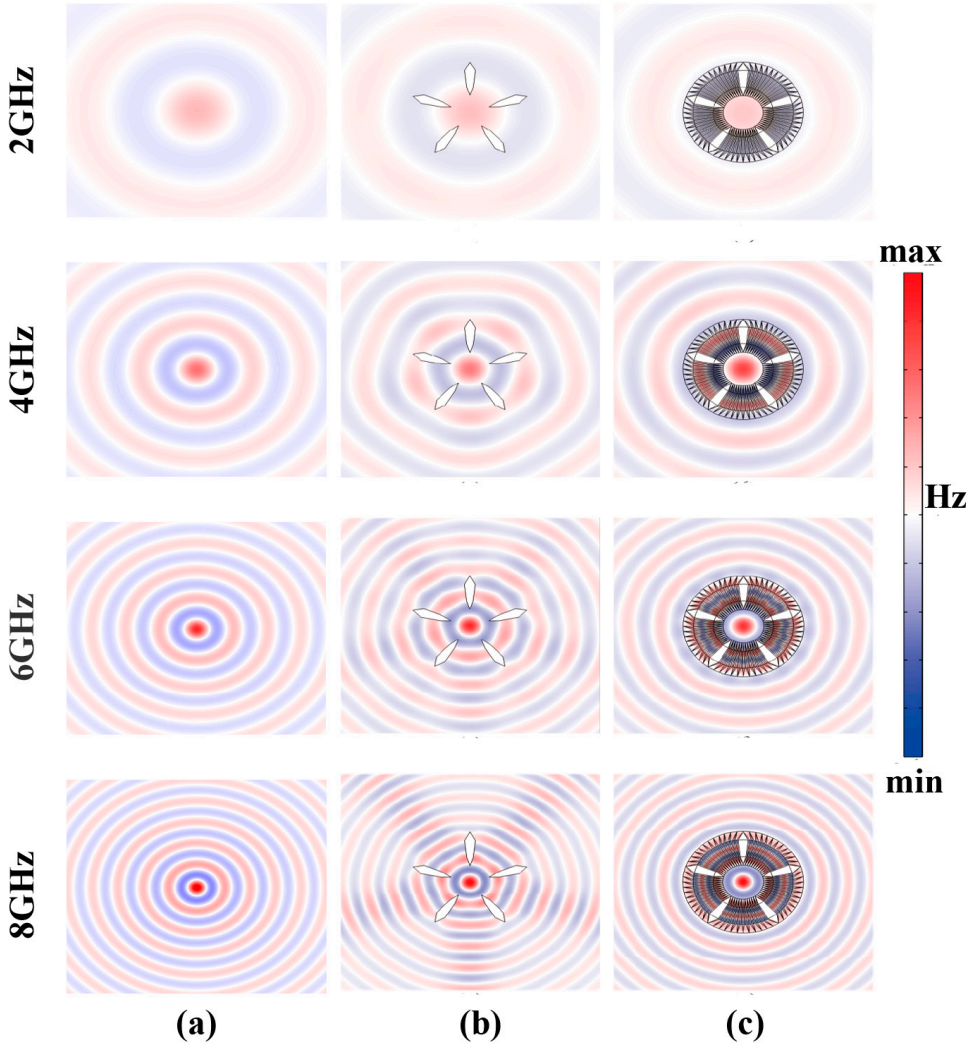


Figure 4. Normalized magnetic field distribution at 2, 4, 6, and 8 GHz from 2D numerical simulation with a centered magnetic current point source. (**a**) Free-space magnetic point source without obstacles; (**b**) magnetic point source surrounded by five PEC obstacles; (**c**) SSC-protected magnetic point source with five PEC obstacles in the concealed regions.

To further validate the applicability of the SSC, we conduct 2D numerical simulations to verify its effectiveness when the point source is offset from the center of the SSC. As shown in rows 1–4 of Figure 5, the magnetic point source is offset to the right by $0.25\lambda_0$ from the center. Figure 5b shows the normalized magnetic field distributions with five PEC obstacles (matching the concealed region geometry) surrounding the

source, where significant radiation pattern distortions caused by scattering from the PEC obstacles are observed at 2, 4, 6, and 8 GHz. However, when the source is surrounded by the SSC (Figure 5c), the electromagnetic waves emitted by the source are guided around the concealed regions and reproduce cylindrical wavefronts at the outer boundary of the SSC across the entire operating bandwidth, protecting the radiation pattern of broadband sources from scattering by obstacles. Notably, the distribution of electromagnetic waves outside the SSC is also offset to the right by $0.25\lambda_0$ relative to the case where the source is at the center of the SSC (Figure 4c). For comparison, Figure 5a shows the free-space magnetic point source without obstacles at corresponding frequencies, exhibiting undistorted cylindrical wavefronts with the wave center offset by $0.25\lambda_0$. To examine the robustness against larger displacements, additional simulations at 8 GHz with the source offset by $0.45\lambda_0$ (approaching the inner boundary) are presented in row 5 of Figure 5. The SSC maintains effective waveguiding and wavefront reconstruction without reflection-induced distortion (Figure 5c, row 5), confirming that the impedance-matching sections l_1 and l_3 preserve entrance matching even for substantial source misalignment. This demonstrates that the SSC remains effective for electromagnetic wave sources located anywhere within its inner boundary.

To quantitatively evaluate the radiation pattern protection performance of the SSC, we introduce the normalized radiation pattern distortion (NRPD), specifically defined for the source-surrounded scenario. Unlike traditional cloaks where normalized scattering cross-section is used for external plane-wave incidence, the NRPD directly measures the distortion of the radiation pattern emitted from an internal source. The NRPD is defined as

$$NRPD_{without\ SSC} = \frac{\int_0^{2\pi} |P_{obstacles}(\phi) - P_{ideal}(\phi)|^2 d\phi}{\int_0^{2\pi} |P_{ideal}(\phi)|^2 d\phi}, \quad (2)$$

$$NRPD_{with\ SSC} = \frac{\int_0^{2\pi} |P_{SSC+obstacles}(\phi) - P_{ideal}(\phi)|^2 d\phi}{\int_0^{2\pi} |P_{ideal}(\phi)|^2 d\phi}. \quad (3)$$

Here $P_{\mathrm{ideal}}(\Phi)$ is the normalized radiation power pattern of the ideal free-space source without obstacles, $P_{\mathrm{obstacles}}(\Phi)$ is the normalized radiation power pattern with obstacles present but without the SSC, and $P_{\mathrm{SSC+obstacles}}(\Phi)$ is the normalized radiation power pattern with both the SSC and obstacles present. The calculation is performed by extracting the Poynting vector radial component $S_r(\Phi)$ along a circular probe at r = 150 mm, with $P(\Phi) = r \cdot S_r(\Phi)$ in the 2D case.

To quantitatively evaluate the broadband radiation pattern protection performance of the SSC, the NRPD is extracted at r = 150 mm across the entire operating bandwidth from 2 to 8 GHz with a frequency step of 0.3 GHz. As shown in Figure 6, the NRPD without the SSC monotonically increases from −16.09 dB at 2 GHz to −3.49 dB at 8 GHz as the wavelength decreases and the scattering by PEC obstacles becomes more severe. In contrast, the NRPD with the SSC remains below −9.33 dB across the entire bandwidth, with an average improvement of 12.15 dB. Notably, the NRPD reaches its minimum of −42.04 dB (0.0063%) at the center frequency of 5 GHz, indicating nearly perfect wavefront reconstruction. The broadband protection is further corroborated by the fact that the NRPD with the SSC falls below −20 dB at seven frequency points (2.0, 2.3, 3.5, 4.7, 5.0, 6.5, and 7.7 GHz), corresponding to the frequencies where the optical path-matching condition is optimally satisfied. A local NRPD minimum of −30.2 dB is also observed at 3.5 GHz, which arises from the constructive interference of the waveguiding channels. It should be noted that a slight NRPD elevation to −9.33 dB occurs at 4.4 GHz, attributed to the reduced transmittance of the AIMM unit cell at this frequency (Figure 2c); nevertheless, the SSC still provides effective radiation pattern protection as the NRPD with the SSC remains lower than that

without the SSC (1.02 dB improvement). These results demonstrate that the SSC achieves consistent radiation pattern protection over the entire 6 GHz bandwidth, validating its broadband and omnidirectional performance for on-chip antenna applications.

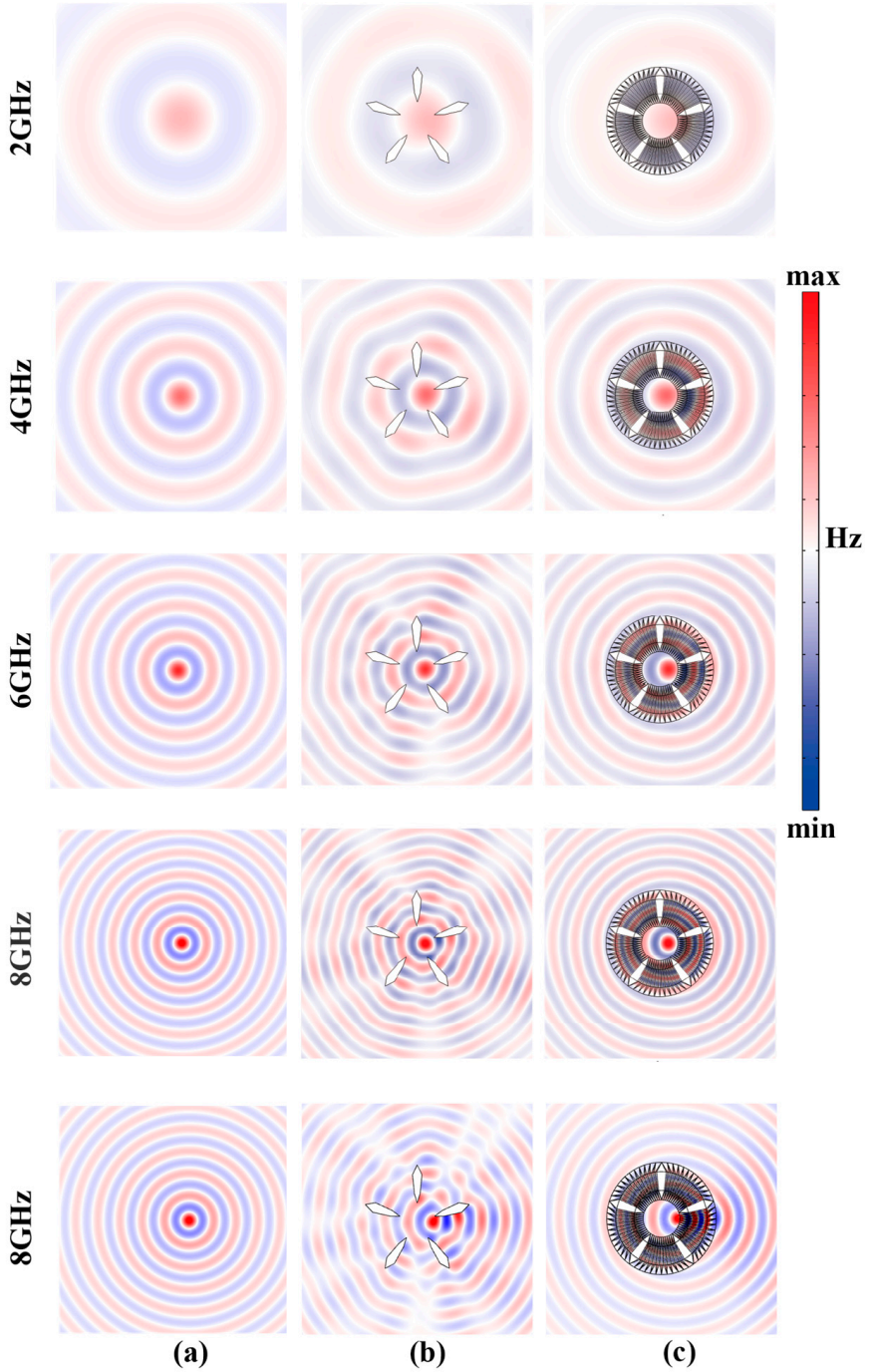


Figure 5. Normalized magnetic field distribution from 2D numerical simulation with the magnetic current point source positioned off-center. Rows 1–4: Source offset by 15 mm ($0.25\lambda_0$) from the center at 2, 4, 6, and 8 GHz, respectively. Row 5: Source offset by 27 mm ($0.45\lambda_0$) from the center at 8 GHz. (**a**) Free-space magnetic point source without obstacles; (**b**) magnetic point source surrounded by five PEC obstacles; (**c**) SSC-protected magnetic point source with five PEC obstacles in the concealed regions.

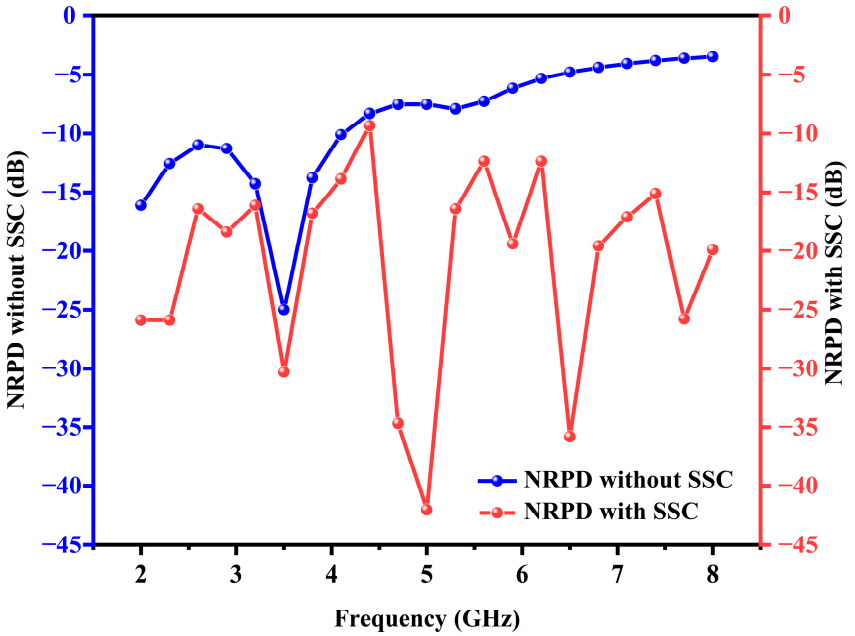


Figure 6. Quantitative evaluation of the broadband SSC performance using NRPD. The NRPD is extracted at r = 150 mm across the 2–8 GHz bandwidth with a frequency step of 0.3 GHz. The blue curve represents the obstacle-only case without SSC, and the red curve represents the SSC-protected case.

4. Discussion

The SSC represents a paradigm shift from traditional external-incidence cloaks to source-surrounded configuration. By guiding outward-propagating waves to bypass obstacles and reconstruct cylindrical wavefronts, it addresses the critical gap where internal sources and scatterers coexist in highly integrated environments. The broadband AIMM achieves a tunable effective refractive index of 1.1–1.5 through geometry-controlled dielectric mixing ratio, avoiding the narrowband limitation of resonant metamaterials. Impedance-matching sections further suppress reflections, ensuring efficient waveguiding even when the source is offset by $0.25\lambda_0$ or $0.45\lambda_0$. Compared with full-space cloaks typically operating at single frequencies and carpet cloaks relying on ground-plane reflections, the SSC provides 6 GHz bandwidth and 360° omnidirectional protection without directional constraints. Future directions include extending the 2D design to three dimensions for arbitrary antenna orientations, experimental validation with fabricated AIMM samples, and scaling to millimeter-wave and terahertz regimes for 5G/6G on-chip communication, Internet-of-Things devices, and high-performance computing modules.

5. Conclusions

In conclusion, in this work, we propose a broadband air-impedance-matched metamaterial over the 2–8 GHz bandwidth that achieves geometry-tunable phase delay with transmittance maintained above 93%. Based on the AIMM, we design an SSC which surrounds the electromagnetic wave source to create five concealed regions. TM electromagnetic waves emitted by the source in any propagation direction can be guided by the SSC to bypass the concealed regions and reproduce the original wavefronts outside the SSC at 2–8 GHz. Thus, it protects the radiation pattern from being distorted by scattering from obstacles. We further validate the applicability of its functionality. Even when the electromagnetic wave source is not strictly centered within the SSC but offset by a certain distance, the SSC still protects the radiation patterns from scattering by obstacles, and the reproduced electromagnetic waves are similarly offset by that distance. It should be clarified that the omnidirectional in-plane emission assumed in this 2D study corresponds to

on-chip magnetic dipole antennas or vertically oriented electric dipoles embedded in planar integrated circuits, which radiate cylindrically within the chip plane. Conventional patch antennas radiating normal to the substrate are outside the scope of this work [57–59]. Our work demonstrates significant potential for enhancing the integration density of integrated circuits and improving the operational stability of communication systems.

Author Contributions: Investigation, W.H. and H.C.; formal analysis, W.H.; validation, W.H.; methodology, W.H. and H.C.; software, W.H. and H.C.; conceptualization, F.S.; writing—original draft preparation, W.H. and H.C.; writing—review and editing, F.S., Y.L. and S.Z.; supervision, F.S. and Y.L.; project administration, F.S.; funding acquisition, F.S., Y.L. and S.Z. All authors have read and agreed to the published version of the manuscript.

Funding: This work is supported by the National Natural Science Foundation of China (Nos. 12274317 and 12374277), San Jin Talent Support Program—Shanxi Provincial Youth Top-notch Talent Project (SJYC2025302), Natural Science Foundation of Shanxi Province (202303021211054), and Shanxi Province Higher Education Institutions Young Faculty Research and Innovation Support Program (2025Q006).

Data Availability Statement: The main data and models supporting the findings of this study are available within the paper. Further information is available from the corresponding authors upon reasonable request.

Conflicts of Interest: The authors declare no competing financial interests.

Abbreviations

The following abbreviations are used in this manuscript:

AIMM	Air-Impedance-Matched Metamaterial
TM	Transverse Magnetic
PEC	Perfect Electric Conductor
SSC	Source-Surrounded Cloak
2D	Two-Dimensional
NRPD	Normalized Radiation Pattern Distortion

References

1. Wang, X.; Han, J.; Tian, S.; Xia, D.; Li, L.; Cui, T.J. Amplification and Manipulation of Nonlinear Electromagnetic Waves and Enhanced Nonreciprocity Using Transmissive Space-Time-Coding Metasurface. *Adv. Sci.* **2022**, *9*, 2105960.
2. Wang, W.; Zheng, Y. Wideband Gain Enhancement of a Dual-Polarized MIMO Vehicular Antenna. *IEEE Trans. Veh. Technol.* **2021**, *70*, 7897–7906. [CrossRef]
3. Zhang, J.; Chen, G.; Yang, M.; Dong, B.; Yang, Y. RIS-Aided Next-Generation High-Speed Train Communications: Challenges, Solutions, and Future Directions. *IEEE Wirel. Commun.* **2021**, *28*, 145–151. [CrossRef]
4. Huang, H.; Chen, H.; Liu, H.; Zhang, Z.; Feng, X.; Chen, J.; Wu, H.; Deng, J.; Liang, W.; Lin, W. High-Intensity Spatial-Mode Steerable Frequency Up-Converter toward On-Chip Integration. *Opto-Electron. Sci.* **2024**, *3*, 230036. [CrossRef]
5. Chen, H.; Liu, Y.; Sun, F.; Sun, Q.; Wu, X.; Sun, R. A Thermal–EM Concentrator for Enhancing EM Signals and Focusing Heat Fluxes Simultaneously. *Laser Photonics Rev.* **2024**, *18*, 2400488. [CrossRef]
6. Liu, Y.; Chen, H.; Sun, F.; Zhang, S. Simultaneously Realizing Thermal and Electromagnetic Cloaking by Multi-Physical Null Medium. *Opto-Electron. Sci.* **2024**, *3*, 230027. [CrossRef]
7. Pendry, J.B.; Schurig, D.; Smith, D.R. Controlling Electromagnetic Fields. *Science* **2006**, *312*, 1780–1782. [CrossRef] [PubMed]
8. Schurig, D.; Mock, J.J.; Justice, B.J.; Cummer, S.A.; Pendry, J.B.; Starr, A.F.; Smith, D.R. Metamaterial Electromagnetic Cloak at Microwave Frequencies. *Science* **2006**, *314*, 977–980. [CrossRef] [PubMed]
9. Sun, R.; Sun, F.; Liu, Y. Research Progress and Development Trend of Electromagnetic Cloaking. *Opto-Electron. Eng.* **2024**, *51*, 240191. [CrossRef]
10. Liu, Y.; Sun, F.; Yang, Y.; Hao, Y.; Liang, S.; Wang, Z. A Metamaterial-Free Omnidirectional Invisibility Cloak Based on Thrice Transformations inside Optic-Null Medium. *Opt. Laser Technol.* **2023**, *157*, 108779. [CrossRef]
11. Zhang, B. Electrodynamics of Transformation-based Invisibility Cloaking. *Light Sci. Appl.* **2012**, *1*, e32. [CrossRef]

12. Xu, L.; Wu, Q.N.; Zhou, Y.Y.; Chen, H.Y. Transformation Devices with Optical Nihility Media and Reduced Realizations. *Front. Phys.* **2019**, *14*, 42501. [CrossRef]
13. Landy, N.; Smith, D.R. A Full-Parameter Unidirectional Metamaterial Cloak for Microwaves. *Nat. Mater.* **2013**, *12*, 25–28. [CrossRef] [PubMed]
14. Zhang, Y.; Luo, Y.; Pendry, J.B.; Zhang, B. Transformation-Invariant Metamaterials. *Phys. Rev. Lett.* **2019**, *123*, 067701. [CrossRef] [PubMed]
15. Sun, F.; Zheng, B.; Chen, H.; Jiang, W.; Guo, S.; Liu, Y.; Ma, Y.; He, S. Transformation Optics: From Classic Theory and Applications to Its New Branches. *Laser Photonics Rev.* **2017**, *11*, 1700034. [CrossRef]
16. Leonhardt, U. Optical Conformal Mapping. *Science* **2006**, *312*, 1777–1780. [CrossRef] [PubMed]
17. Leonhardt, U.; Tyc, T. Broadband Invisibility by Non-Euclidean Cloaking. *Science* **2009**, *323*, 110–112. [CrossRef] [PubMed]
18. Xu, L.; Chen, H. Conformal Transformation Optics. *Nat. Photonics* **2015**, *9*, 15–19. [CrossRef]
19. Xu, L.; Chen, H. Transformation metamaterials. *Adv. Mater.* **2021**, *33*, 2005489. [CrossRef]
20. Alù, A.; Engheta, N. Plasmonic Materials in Transparency and Cloaking Problems: Mechanism, Robustness, and Physical Insights. *Opt. Express* **2007**, *15*, 3318–3332. [CrossRef] [PubMed]
21. Alù, A.; Engheta, N. Multifrequency Optical Invisibility Cloak with Layered Plasmonic Shells. *Phys. Rev. Lett.* **2008**, *100*, 113901. [CrossRef] [PubMed]
22. Alù, A. Mantle cloak: Invisibility Induced by a Surface. *Phys. Rev. B* **2009**, *80*, 245115. [CrossRef]
23. Soric, J.; Ra'di, Y.; Farfan, D.; Alù, A. Radio-transparent Dipole Antenna Based on a Metasurface Cloak. *Nat. Commun.* **2022**, *13*, 1114. [CrossRef] [PubMed]
24. Arango, F.B.; Alpeggiani, F.; Conteduca, D.; Opheij, A.; Chen, A.; Abdelrahman, M.I.; Krauss, T.F.; Alù, A.; Monticone, F.; Kuipers, L. Cloaked Near-Field Probe for Non-Invasive Near-Field Optical Microscopy. *Optica* **2022**, *9*, 684. [CrossRef]
25. Jiang, Z.; Sieber, P.E.; Kang, L.; Werner, D.H. Restoring Intrinsic Properties of Electromagnetic Radiators Using Ultralightweight Integrated Metasurface Cloaks. *Adv. Funct. Mater.* **2015**, *25*, 4708–4716. [CrossRef]
26. Zheng, B.; Chen, X.; Liu, C.; Wang, Y.; Zhang, B. Experimental Realization of an Extreme-Parameter Omnidirectional Cloak. *Research* **2019**, *2019*, 8282641. [CrossRef] [PubMed]
27. Gao, Y.; Li, Y.; Zhang, Y.; Zhang, B. Full-parameter Omnidirectional Transformation Optical Devices. *Natl. Sci. Rev.* **2024**, *11*, nwad171. [PubMed]
28. Hu, X.; Li, J.; Wang, Z.; Jia, Y.; Liu, F. Multiband Omnidirectional Invisibility Cloak. *Adv. Sci.* **2024**, *11*, 2401295. [CrossRef]
29. Sun, F.; Liu, Y.; He, S. Surface transformation Multi-Physics for Controlling Electromagnetic and Acoustic Waves Simultaneously. *Opt. Express* **2019**, *28*, 94–104. [CrossRef]
30. Hu, X.; Luo, Y.; Tang, J.; Wang, C.; Gao, Y.; Zhang, J.; Zhang, Y.; Ye, D. Breaking Bandwidth Limits in Transformation Optics with Brewster-Enhanced Metamaterials. *Natl. Sci. Rev.* **2026**, *13*, nwag023. [CrossRef] [PubMed]
31. Liu, R.; Ji, C.; Mock, J.J.; Chin, J.Y.; Cui, T.J.; Smith, D.R. Broadband Ground-Plane Cloak. *Science* **2009**, *323*, 366–369. [CrossRef] [PubMed]
32. Li, J.; Pendry, J.B. Hiding under the Carpet: A New Strategy for Cloaking. *Phys. Rev. Lett.* **2008**, *101*, 203901. [CrossRef] [PubMed]
33. Ma, H.F.; Cui, T.J. Three-Dimensional Broadband Ground-Plane Cloak Made of Metamaterials. *Nat. Commun.* **2010**, *1*, 21. [CrossRef] [PubMed]
34. Zhao, J.; Zhu, P.; Wen, Z.; Tang, F.; Zheng, B.; Zhu, R.; Qian, H.; Qian, C.; Lu, H. Adaptive Transparent Cloaking Tunnel Enabled by Meta-Reinforcement-Learning Metasurfaces. *PhotoniX* **2026**, *7*, 2. [CrossRef]
35. Wu, B.; Qian, C.; Wang, Z.; Lin, P.; Li, E. MetaSeeker: Sketching an Open Invisible Space with Self-Play Reinforcement Learning. *Light Sci. Appl.* **2025**, *14*, 211. [CrossRef] [PubMed]
36. Deng, Y.; Liu, Z.; Song, C.; Wu, J.; Liu, Y.; Wu, Y. Topology Optimization Based Computational Design Methodology for Surface Plasmon Polaritons. *Plasmonics* **2015**, *10*, 569–583. [CrossRef]
37. Deng, Y.; Korvink, J.G. Topology Optimization for Three-Dimensional Electromagnetic Waves Using an Edge Element-Based Finite-Element Method. *Proc. R. Soc. A* **2016**, *472*, 20150835. [CrossRef] [PubMed]
38. Deng, Y. *Adjoint Topology Optimization Theory for Nano-Optics*; Springer: Singapore, 2022.
39. Rane, S.; Prabhu, S.; Chowdhury, D.R. Physics and Applications of Terahertz Metagratings. *Opto-Electron. Sci.* **2024**, *3*, 230049. [CrossRef]
40. Zhao, S.; Fan, Y.; Yang, R.; Ye, Z.; Zhang, F.; Wang, C.; Luo, W.; Wen, Y.; Zhou, J. Smart Reconfigurable Metadevices Made of Shape Memory Alloy Metamaterials. *Opto-Electron. Adv.* **2025**, *8*, 240109. [CrossRef]
41. Sun, F.; Zhang, H.; Liu, Y.; Qin, W.; Li, D. Multiphysics Metamaterials for Unified Control of Diverse Physical Fields. *Small Struct.* **2025**, *6*, 2500352. [CrossRef]
42. Chen, Z.; Sun, F.; Liu, Y.; Ma, X.; Chen, H.; Chao, K.; Chen, Z.; Wang, J. Electromagnetic-Acoustic Splitter with a Tunable Splitting Ratio Based on Copper Plates. *Opt. Lett.* **2023**, *48*, 3407–3410. [CrossRef] [PubMed]

43. Zhang, Z.; Xu, L.; Qu, T.; Lei, M.; Lin, Z.-K.; Ouyang, X.; Jiang, J.-H.; Huang, J. Diffusion Metamaterials. *Nat. Rev. Phys.* **2023**, *5*, 218–235. [CrossRef]
44. Liu, Z.; Jin, P.; Lei, M.; Wang, C.; Zhuang, P.; Tan, P.; Jiang, J.-H.; Marchesoni, F.; Huang, J. Topology in Thermal, Particle, and Plasma Diffusion Metamaterials. *Chem. Rev.* **2025**, *125*, 8655–8730. [CrossRef] [PubMed]
45. Yang, F.; Zhang, Z.; Xu, L.; Liu, Z.; Jin, P.; Zhuang, P.; Lei, M.; Liu, J.; Jiang, J.-H.; Ouyang, X.; et al. Controlling Mass and Energy Diffusion with Metamaterials. *Rev. Mod. Phys.* **2024**, *96*, 015002. [CrossRef]
46. Shi, H.T.; Zhang, L.; Wu, R.Y.; Zheng, Y.N.; Chen, X.Q.; Li, Y.; He, S.; Wu, J.W.; Cheng, Q.; Cui, T.J. Programmable Calculus Operations in Electromagnetic Space Using Space-Time-Coding Metasurface. *Natl. Sci. Rev.* **2026**, *13*, nwag249. [PubMed]
47. Zhang, L.; Cui, T.J. Space-Time-Coding Digital Metasurfaces: Principles and Applications. *Research* **2021**, *2021*, 9802673. [CrossRef] [PubMed]
48. Garg, P.; Lamprianidis, A.G.; Beutel, D.; Karamanos, T.; Verfürth, B.; Rockstuhl, C. Modeling Four-Dimensional Metamaterials: A T-Matrix Approach to Describe Time-Varying Metasurfaces. *Opt. Express* **2022**, *30*, 45832–45847. [CrossRef] [PubMed]
49. Liu, Y.; Deng, R.; Sun, F. Virtual Fresnel Drag in Spatiotemporal Transformation Medium. *Opt. Express* **2024**, *32*, 32128–32137. [CrossRef] [PubMed]
50. Engheta, N. Four-Dimensional Optics Using Time-Varying Metamaterials. *Science* **2023**, *379*, 1190–1191. [CrossRef] [PubMed]
51. Lu, J.; Deng, W.; Huang, X.; Ke, M.; Liu, Z. Non-Hermitian Topological Phononic Metamaterials. *Adv. Mater.* **2025**, *37*, 2307998. [CrossRef] [PubMed]
52. Zhou, D.; Zhang, J. Non-Hermitian Topological Metamaterials with Odd Elasticity. *Phys. Rev. Res.* **2020**, *2*, 023173. [CrossRef]
53. Liu, Y.; Qi, Y.; Sun, F.; Shan, J.; Chen, H.; Hao, Y.; Fei, H.; Cao, B.; Liu, X.; Huo, Z. Active Thermal Metasurfaces Enable Superscattering of Thermal Signatures Across Arbitrary Shapes and Thermal Conductivities. *Adv. Sci.* **2025**, *13*, e19386. [CrossRef]
54. Liu, Z.; Jin, P.; Lei, M.; Wang, C.; Marchesoni, F.; Jiang, J.-H.; Huang, J. Topological Thermal Transport. *Nat. Rev. Phys.* **2024**, *6*, 554–565. [CrossRef]
55. Liu, Y.; Chao, K.; Sun, F.; Chen, S.; Dai, H.; Chen, H. Active Thermal Metasurfaces for Remote Heating/Cooling by Mimicking Negative Thermal Conductivity. *Adv. Mater.* **2023**, *35*, 2210981. [CrossRef]
56. Penn, S.J.; Birchall, J.K.; Bridger, D.C.; Readey, C.W. Effect of Porosity and Grain Size on the Microwave Dielectric Properties of Sintered Alumina. *J. Am. Ceram. Soc.* **1997**, *80*, 1885–1888. [CrossRef]
57. Alibakhshikenari, M.; Ali, E.M.; Soruri, M.; Dalarsson, M.; Naser-Moghadasi, M.; Virdee, B.S.; Stefanovic, C.; Pietrenko-Dabrowska, A.; Koziel, S.; Szczepanski, S.; et al. A Comprehensive Survey on Antennas On-Chip Based on Metamaterial, Metasurface, and Substrate Integrated Waveguide Principles for Millimeter-Waves and Terahertz Integrated Circuits and Systems. *IEEE Access* **2022**, *10*, 3668–3692. [CrossRef]
58. Guo, J.; Bai, H.; Feng, A.; Liu, Y.; Huang, Y.; Zhang, X. A Compact Dual-Band Slot Antenna with Horizontally Polarized Omnidirectional Radiation. *IEEE Antennas Wirel. Propag. Lett.* **2021**, *20*, 1234–1238. [CrossRef]
59. Asfour, R.; Khamas, S.K.; Ball, E.A.; Ng, J.S.; Huang, G.; Allanic, R.; Le Berre, D.; Quendo, C.; Leuliet, A.; Merlet, T. On-Chip Circularly Polarized Circular Loop Antennas Utilizing 4H-SiC and GaAs Substrates in the Q/V Band. *Sensors* **2024**, *24*, 321. [CrossRef] [PubMed]

Disclaimer/Publisher's Note: The statements, opinions and data contained in all publications are solely those of the individual author(s) and contributor(s) and not of MDPI and/or the editor(s). MDPI and/or the editor(s) disclaim responsibility for any injury to people or property resulting from any ideas, methods, instructions or products referred to in the content.